nature portfolio

https://doi.org/10.1038/s41565-022-01144-x

Supplementary information

Current-driven dynamics and ratchet effect of skyrmion bubbles in a ferrimagnetic insulator

In the format provided by the authors and unedited

Supplementary Information for

Current-driven dynamics and ratchet effect of skyrmion bubbles in a ferrimagnetic insulator

Saül Vélez[1,5,*], Sandra Ruiz-Gómez[2,3,6], Jakob Schaab[1], Elzbieta Gradauskaite[1], Martin S. Wörnle[4], Pol Welter[4], Benjamin J. Jacot[1], Christian L. Degen[4], Morgan Trassin[1], Manfred Fiebig[1] & Pietro Gambardella[1,*]

[1] Department of Materials, ETH Zurich, 8093 Zurich, Switzerland

[2] Departamento de Física de Materiales, Universidad Complutense de Madrid, 28040 Madrid, Spain

[3] Alba Synchrotron Light Facility, 08290, Cerdanyola del Valles, Barcelona, Spain

[4] Department of Physics, ETH Zurich, 8093 Zurich, Switzerland

[5] Present address: Condensed Matter Physics Center (IFIMAC), Instituto Nicolás Cabrera, and Departamento de Física de la Materia Condensada, Universidad Autónoma de Madrid, 28049 Madrid, Spain

[6] Present address: Max Planck Institute for Chemical Physics of Solids, 01187 Dresden, Germany

[*]e-mail: saul.velez@uam.es (S.V.); pietro.gambardella@mat.ethz.ch (P.G.)

Table of contents:

Supplementary Note 1. Structural and topographic characterization of YIG/TmIG and YIG/TmIG/Pt

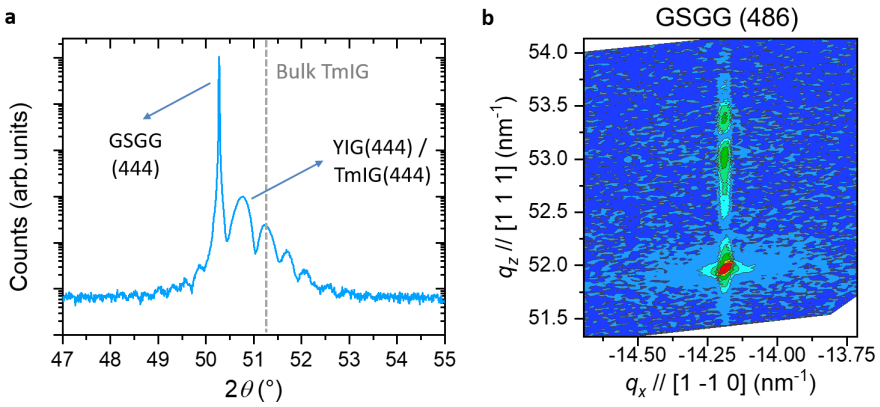

Supplementary Figure 1 | Structural characterization of the YIG/TmIG films. **a**, Symmetric X-ray diffraction scan of the GSGG/YIG(10 nm)/TmIG(20 nm) sample investigated in this work. As the X-ray response of a 10-nm-thick YIG is relatively weak[1], the signal in YIG/TmIG is dominated by the TmIG (444) diffraction peak and corresponding Laue oscillations. The peak shifts towards higher angles with respect to the bulk value[2] (dashed grey line) because of a reduction of the out-of-plane lattice constant due to tensile strain, in agreement with previous reports of TmIG films grown on GSGG[3,4]. **b**, Reciprocal space maps of the same sample around the GSGG (486) substrate peak (q_x and q_z are the in-plane and out-of-plane wavevectors along the crystal axes indicated). The in-plane lattice constants of the films and the substrate along the [1 -1 0] direction coincide, confirming full epitaxy. The colour code indicates the intensity of the diffraction peaks, with red (blue) corresponding to maximum (minimum) intensity.

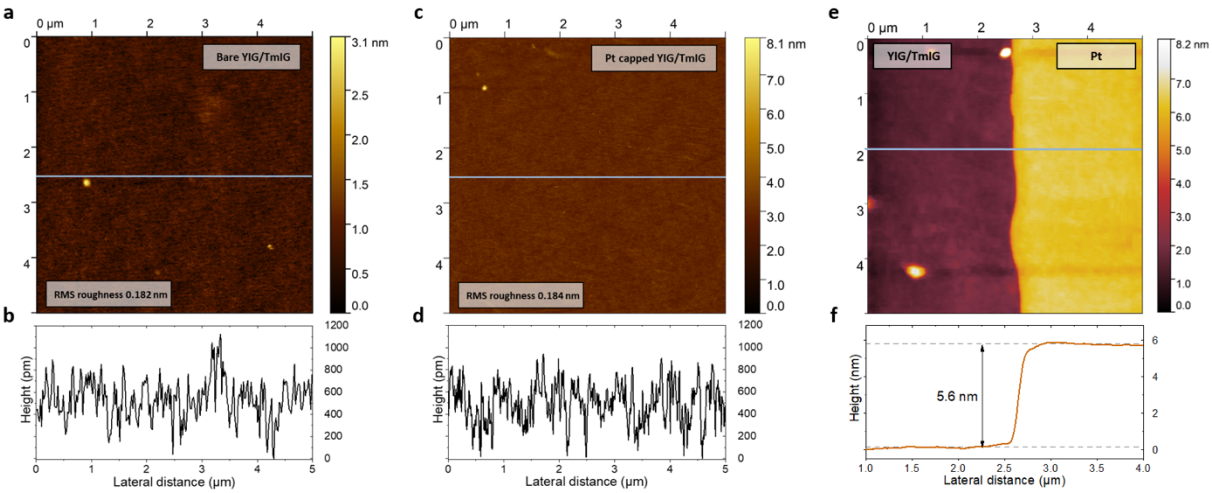

Supplementary Figure 2 | Topographic characterization of YIG/TmIG and YIG/TmIG/Pt. a, **c**, Atomic force microscopy (AFM) characterization of the surface topography of a bare YIG/TmIG and a Pt-capped YIG/TmIG heterostructure, respectively. The root mean square (RMS) roughness over a $\sim 5 \times 5$ μm^2 area is on the order of 0.182 and 0.184 nm, respectively. **b**, **d**, AFM line profiles along the blue lines indicated in **a** and **c**, respectively, confirming the low roughness of our YIG/TmIG and YIG/TmIG/Pt films. **e**, AFM scan of the sample studied in the main text in a region partially covered with Pt. **f**, Average topography scan of the Pt edge along the blue line indicated in **e**, showing that the step size is about 5.6 nm. Consequently, we estimate the etching of the TmIG thickness in $\sim$0.5 nm. The RMS surface roughness is below 0.2 nm on both the etched and Pt covered regions.

Supplementary Note 2. Magnetic characterization of YIG/TmIG

The magnetic anisotropy and saturation magnetization of the YIG(10nm)/TmIG(20nm)/Pt sample investigated in this work have been characterized by a combination of superconducting quantum interference device (SQUID) magnetometry and spin Hall magnetoresistance (SMR) measurements[3,5,6].

Magnetic anisotropy. Supplementary Figure 3 shows that the TmIG layer exhibits perpendicular magnetic anisotropy, with an effective anisotropy field $H_{\mathrm{k}} \sim 1.4$ kOe, and that the YIG layer exhibits an easy-plane anisotropy with a part of the film rotating towards out-of-plane due to the exchange coupling with TmIG.

The smaller (larger) magnetic field required for saturating the magnetization in the out-of-plane (in-plane) configuration indicates that the dominant magnetic anisotropy of YIG/TmIG is out of plane (Supplementary Figs. 3a,3b). As SMR is only sensitive to the magnetic moments at the metal/insulator interface, the magnetic anisotropy of TmIG can be directly proven via transport measurements[3,4]. Supplementary Fig. 3c demonstrates that the magnetization of TmIG points out of plane at zero field, and gradually cants towards the plane as the in-plane field increases. From these measurements, we determine that the magnetic anisotropy of the bilayer is dominated by the perpendicular magnetic anisotropy of TmIG, which corresponds to an anisotropy field $H_{\mathrm{k}} \sim 1.4$ kOe.

The small magnetic moment of the hysteresis loop for the in-plane measurement ($\sim 1.2 \times 10^{-8}$ A m^2 at zero field, Supplementary Fig. 3b) relative to the saturation magnetic moment of the full heterostructure ($\sim 7.7 \times 10^{-8}$ A m^2, Supplementary Fig. 3a) indicates that part of the YIG film magnetization lies in the plane of the film. This is not surprising, as YIG on GSGG is expected to exhibit in-plane anisotropy. From comparing the in-plane and out-of-plane data, we estimate that the magnetization of the first ~ 3 nm of YIG on GSGG lies in the plane of the film, while the rest gradually rotates towards out of the plane due to the exchange coupling with TmIG. The gradual increase of the magnetic moment with field above $H \sim 70$ Oe, Supplementary Fig. 3b, is consistent with the in-plane magnetic field gradually canting the magnetic moments of both the exchange-coupled YIG and the TmIG layer towards the plane, eventually achieving full saturation at ~ 1.4 kOe (Supplementary Fig. 3c; the relatively large paramagnetic response of GSGG prevents us to extract the saturation field from SQUID measurements). Importantly, the magnetic jump observed around zero field for the in-plane configuration indicates that the bottom part of the YIG film can be oriented with relatively small in-plane fields (~ 5 Oe; see inset of Supplementary Fig. 3b). This allows for controlling the sign of the exchange field between YIG and TmIG, a result that is in agreement with the ratchet effect presented in Figs. 5 and 6 of the main text as well as Supplementary Notes 9 and 10.

Saturation magnetization. From the measurements shown in Supplementary Fig. 3, we estimate that the saturation magnetic moment of YIG(10nm)/TmIG(20nm) is $\sim 7.7 \times 10^{-8}$ A m^2. Taking into account that the surface area of the films is ~ 26 mm^2, and assuming that the saturation magnetization of the YIG film is $M_{\mathrm{S}}(\mathrm{YIG}) \sim 175$ kA m^{-1} (Ref. [7]), we estimate the saturation magnetization of TmIG to be $M_{\mathrm{S}}(\mathrm{TmIG}) \sim 60$ kA m^{-1}.

Temperature dependence. The saturation magnetization reduces by about 18% when increasing the temperature from 300 to 350 K (Supplementary Fig. 4). We thus estimate that the TmIG magnetization

decreases by a maximum of 7% due to Joule heating in the current-induced skyrmion dynamics experiments (see Extended Data Fig. 4 for the analysis of the current-induced Joule heating).

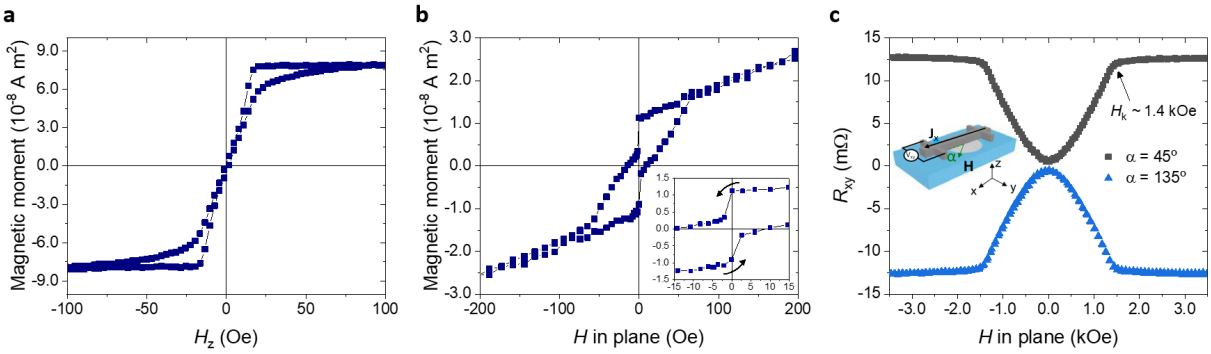

Supplementary Figure 3 | Magnetic characterization of YIG(10nm)/TmIG(20nm). **a**, Magnetic moment of the heterostructure as a function of out-of-plane field H_z. Both layers are fully saturated out of plane at $H_z \sim 100$ Oe. Note that the coercive field is smaller than the one shown in Fig. 1b of the manuscript. The larger coercive field in Fig. 1b is due to the pinning of domain walls at the device edges, resulting in a broadening of the hysteresis loop at the device area[3]. **b**, Magnetic moment as a function of in-plane field. *Inset*, magnification of the loop around zero field. The paramagnetic response of the GSGG substrate has been subtracted in **a** and **b**. **c**, Transverse SMR measurements as a function of in-plane field applied at an angle α with respect to the current direction. From these measurements, we can extract the magnetic anisotropy of TmIG[3,5,6]. At $H = 0$, $R_{xy} \approx 0$, indicating that the local magnetic moments of TmIG point out of the plane and are mostly randomly oriented, which is consistent with the data in **a** and the bottom images of Fig. 1c,d of the manuscript. As H increases, the magnetization of TmIG cants towards the plane, resulting in a change of the amplitude of R_{xy}, which is maximum at $\alpha = 45°$ (positive change) or $135°$ (negative change). The saturation of R_{xy} above $H_k \sim 1.4$ kOe indicates that the magnetic moments of TmIG are saturated in-plane, thus identifying H_k as the anisotropy field of TmIG. We remark that H_k is about half the value measured for single-layer TmIG films of the same thickness on GSGG[3,4], evidencing the role of the exchange coupling with YIG on the magnetic anisotropy of TmIG. Note that each measurement consists of superposed forward and backward field sweeps, indicating that the canting of the magnetic moments of TmIG does not exhibit hysteresis. A device-dependent constant offset is subtracted in **c** for convenience.

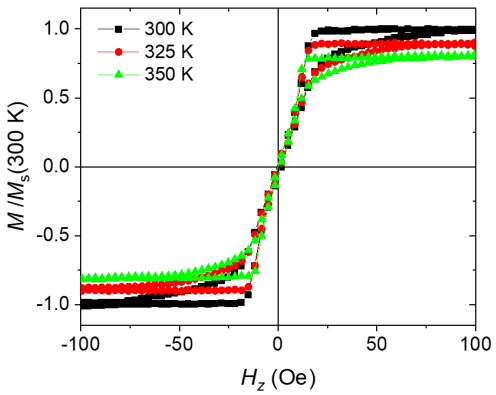

Supplementary Figure 4. Temperature dependence of the out-of-plane magnetization. The data are normalized to the saturation magnetization M_s at 300 K.

Supplementary Note 3. Chirality determination via nitrogen-vacancy magnetometry

We used nitrogen-vacancy (NV) scanning magnetometry to characterize isolated skyrmion bubbles. This technique measures the stray field B_{NV} produced by the magnetic textures of the sample at the position of the NV center with high field and spatial resolution, from which the spin texture of domain walls and skyrmions can be determined[3,8,9]. Figures 2a,d of the manuscript and Supplementary Fig. 6a show representative stray field scanning maps $B_{\mathrm{NV}}(X,Y)$ of bubble domains located in YIG/TmIG/Pt and of a stripe domain intersecting a region partially covered by Pt.

Skyrmion bubbles modelling. We model the skyrmion as a closed ring of ellipsoidal shape, arbitrary orientation β, diametral axes a and b, center X_0, Y_0, and wall width Δ_{DW}. By adapting previous modelling of straight domain walls[3] to the bubble case, the domain wall profile is described by

$$M_X(r) = M_s \frac{\cos\psi}{\cosh\left(\frac{r-r_0}{\Delta_{\mathrm{DW}}}\right)}$$

$$M_Y(r) = M_s \frac{\sin\psi}{\cosh\left(\frac{r-r_0}{\Delta_{\mathrm{DW}}}\right)},$$

$$M_Z(r) = -M_s \tanh\left(\frac{r-r_0}{\Delta_{\mathrm{DW}}}\right), \qquad (1)$$

where r_0 indicate the position of the center of the wall for a given position along the wall ring of the bubble, r the position in the direction perpendicular to the domain wall for the corresponding r_0, and ψ is the chiral angle that describes the magnetic texture of the wall.

To fit the data, we normalized $B_{\mathrm{NV}}(X,Y)$ to the maximum value to remove the influence of YIG on the stray field of TmIG. The fitting procedure is done by first finding the best domain wall width Δ_{DW} for a given domain wall type (Bloch, righ-handed Néel, and left-handed Néel), leaving a, b, and β as free parameters. In a second step, Δ_{DW} is fixed and a, b, and β (if $a \neq b$) are fitted. As an example, Fig. 2b of the manuscript shows the best fit of the stray field data presented in Fig. 2a, which corresponds to a circular bubble with right-handed Néel chirality, $\Delta_{\mathrm{DW}} = 60$ nm, and $a \sim b = 950$ nm. The accuracy of the fitting is computed from the residual sum of squares (RSS) using following formula

$$\ln \mathcal{L}_1 - \ln \mathcal{L}_2 = -\frac{n}{2} \ln \frac{\mathrm{RSS}_1}{\mathrm{RSS}_2}, \qquad (2)$$

where 1 and 2 indicate different sets of fit parameters with 2 being the one with smallest RSS, and n the number of data points. Therefore, by using Supplementary Eq. (2) with different fit parameters, one can estimate the likelihood of a given type of domain wall. Supplementary Fig. 5 presents the likelihood of fitting the skyrmion data of Fig. 2a of the manuscript to different domain wall types characterized by ψ and Δ_{DW}. The likelihood plot clearly shows that the right-handed Néel chirality is the spin texture that best describes the skyrmions for wall widths in the range from $\Delta_{\mathrm{DW}} \sim 30$ to ~ 100 nm, with best fit obtained with $\Delta_{\mathrm{DW}} = 60$ nm. Taking into account the magnetic anisotropy of the film (Supplementary Note 2) and previous characterization of the domain wall width in TmIG[3], we expect the domain wall width to be about 50 nm. We thus conclude that in YIG/TmIG/Pt the domain

wall texture is of right-handed Néel type. The same fitting procedure was followed for the deformed skyrmion presented in Fig. 2d-f of the manuscript.

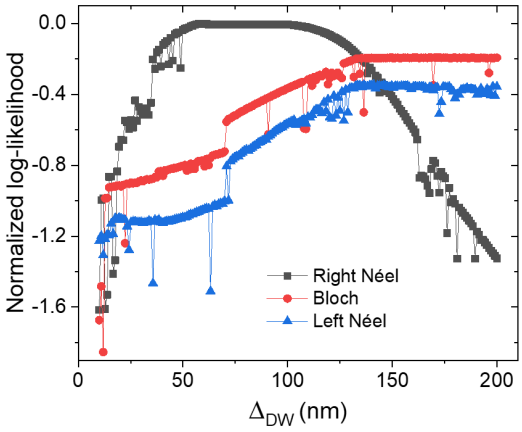

Supplementary Figure 5 | Log-likelihood of the fits of the data of Fig. 2a computed using Supplementary Eq. (2). Different Δ_{DW} values from 10 to 200 nm and different domain wall textures (Bloch, right-handed Néel, and left-handed Néel) were considered.

Analysis of straight domain walls in YIG/TmIG/Pt and YIG/TmIG. To infer the contribution of the YIG/TmIG interface to the DMI, we performed measurements of the stray field of a narrow stripe domain running across a region partially covered by Pt (Supplementary Fig. 6a). Direct inspection reveals that the stray field in the Pt-covered region is stronger than in the Pt-free region (Supplementary Fig. 6b). However, as we demonstrated in an earlier work, Pt also contributes to the stray field due to the magnetization induced by proximity with TmIG[3]. Therefore, for comparing the data, we subtracted the stray field associated to the Pt polarization in the YIG/TmIG/Pt region. The normalized line scans are very similar (Supplementary Fig. 6c), indicating that the domain wall type in YIG/TmIG is also right-handed Néel (as determined to be for YIG/TmIG/Pt; Fig. 2 and Supplementary Fig. 5) or of intermediate right-handed Néel-Bloch favored by a positive DMI induced by the YIG interface. Note that changes in Δ_{DW} between the Pt-capped and Pt-free regions are expected to be negligible[10], and thus no significant influence of Δ_{DW} on the stray field is expected. The relatively large uncertainty of the stray field data, however, does not allow us to conclude on the precise value of ψ. Nevertheless, the right-handed chirality in GSGG/YIG/TmIG is clearly different from that of TmIG directly grown on GSGG, which presents negative DMI and left-handed Néel domain walls[3]. As the TmIG/Pt interface has a positive DMI[3], we conclude that both YIG and Pt interfaces contribute to stabilize right-handed Néel domain walls and skyrmions in TmIG with an overall DMI strength above D_{th}.

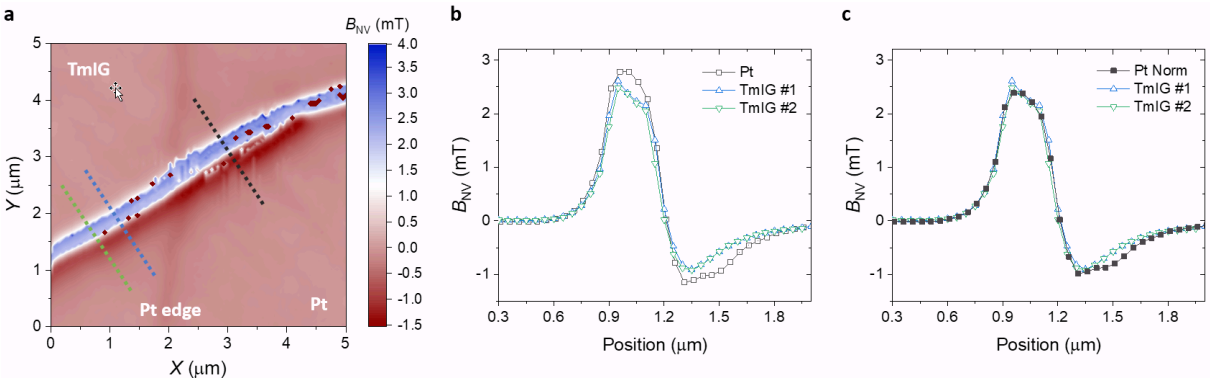

Supplementary Figure 6 | Comparison of the stray field of a stripe domain in a region partially covered by Pt. **a**, Stray field map $B_{\mathrm{NV}}(XY)$ of a stripe domain running across a region partially covered with Pt. Note that the stray field arises from two parallel domain walls. $|H_{\mathrm{z}}| = 15$ Oe. **b**, Line scans of B_{NV} along the dashed lines in **a** (open symbols; the colour code identifies the line scan). **c**, Same as in **b** with the stray field in the Pt region corrected by the contribution of the Pt polarization to the stray field[3] (solid black symbols).

Supplementary Note 4. Determination of the effective g factor of TmIG

To estimate the effective g factor of TmIG we used the Wangsness relation[11,12]

$$\frac{M_{\mathrm{Fe}}}{g_{\mathrm{Fe}}} - \frac{M_{\mathrm{Tm}}}{g_{\mathrm{Tm}}} = \frac{M_s}{g}, \tag{3}$$

where M_{Fe} and g_{Fe} are the magnetic moment and g factor of the Fe^{3+} tetrahedral/octahedral sublattices, M_{Tm} and g_{Tm} the magnetic moment and g factor of the Tm^{3+} dodecahedral sublattice, and $M_{\mathrm{s}} = M_{\mathrm{Fe}} - M_{\mathrm{Tm}}$ and g the net magnetic moment and effective g factor of TmIG. The negative sign accounts for the antiferromagnetic coupling between the Fe^{3+} and Tm^{3+} sublattices with both M_{Fe} and M_{Tm} defined positive and $M_{\mathrm{Fe}} > M_{\mathrm{Tm}}$. We take $g_{\mathrm{Fe}} = 2$ (Ref. 7) and estimate g_{Tm} from the expected g factor of a free Tm^{+3} ion. At the lowest spin-orbit multiplet state, the total angular momentum of Tm^{3+} is $J = 6$ with an orbital momentum $L = 1$ and spin state $S = 5$, resulting in $g_{\mathrm{Tm}} = 7/6$. The saturation magnetization of TmIG is estimated to be $M_{\mathrm{s}} \sim 60$ kA m^{-1} (see Supplementary Note 2).

In thin films, M_{Fe} and M_{Tm} may substantially deviate from the bulk values due to strain and finite size effects[1,3,7,13], giving a wide range of possible $M_{\mathrm{Fe}}, M_{\mathrm{Tm}}$ values for the solution of Supplementary Eq. (3). Supplementary Fig. 7 shows the value of g computed by using Supplementary Eq. (3) and considering different combinations of M_{Fe} and M_{Tm} values. g_{Fe} and g_{Tm} are constrained to be 2 and 7/6, respectively. The dashed line indicates combinations with $M_{\mathrm{Fe}} - M_{\mathrm{Tm}} = 60$ kA m^{-1}. The bluish-coloured area corresponds to solutions with negative g values, which is the case expected for our TmIG film according to the sign of the skyrmion Hall effect (Fig. 3 of the main text). By fixing M_{Fe} to be 175 kA m^{-1} (Ref. 7), we estimate $M_{\mathrm{Tm}} \sim 115$ kA m^{-1} and $g \sim -5.4$ (solution indicated by a blue dot in Supplementary Fig. 7).

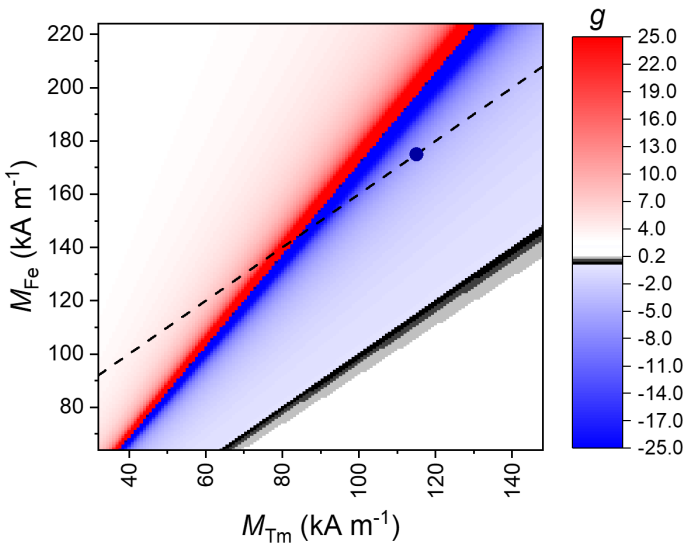

Supplementary Figure 7 | Computed g values of TmIG for different M_{Fe} and M_{Tm} combinations. Computed g values by using Supplementary Eq. (3) and $g_{\mathrm{Fe}} = 2$ and $g_{\mathrm{Tm}} = 7/6$. The dashed line indicates $M_{\mathrm{Fe}}, M_{\mathrm{Tm}}$ combinations with constant $M_{\mathrm{s}} = 60$ kA m^{-1}. The blueish region corresponds to solutions with $g < 0$. The blue dot indicates the combination $M_{\mathrm{Fe}} = 175$ kA m^{-1} and $M_{\mathrm{Tm}} = 115$ kA m^{-1}, which results in $g = -5.4$. See text for more details.

Supplementary Note 5. Thiele's equation of a ferrimagnet and skyrmion velocity

Thiele's equation. Under the approximation of point-like massless objects, the dynamics of skyrmions driven by current pulses is described by the modified Thiele's equation[14,15,16]

$$\mathbf{G} \times \mathbf{v}_{\mathrm{sk}} - \alpha \boldsymbol{\mathcal{D}} \mathbf{v}_{\mathrm{sk}} + \mathbf{F}_{\mathrm{SOT}} = 0, \tag{4}$$

where $\mathbf{G} = G\hat{\boldsymbol{z}}$ is the gyromagnetic vector, $\mathbf{v}_{\mathrm{sk}} = v_x\hat{\boldsymbol{x}} + v_y\hat{\boldsymbol{y}}$ the skyrmion velocity, α the damping parameter, $\boldsymbol{\mathcal{D}}$ the dissipative tensor, and $\mathbf{F}_{\mathrm{SOT}} = F_{\mathrm{SOT}}\hat{\boldsymbol{x}}$ the SOT driving force generated by $\mathbf{J}_x = J_x\hat{\boldsymbol{x}}$ (see Supplementary Fig. 8 for the schematics of the forces). $\hat{\boldsymbol{x}}$, $\hat{\boldsymbol{y}}$, and $\hat{\boldsymbol{z}}$ are unit vectors along the x, y, and z directions, respectively. The gyromagnetic vector is given by

$$G = -4\pi \frac{M_{\mathrm{s}} t}{\gamma}\, Q, \tag{5}$$

where M_{s}, t, and $\gamma = g\frac{\mu_B}{\hbar}$ are the saturation magnetization, thickness, and gyromagnetic factor of the magnetic layer, g the Landé g factor, and $Q = \frac{1}{4\pi}\iint \left\{\left(\frac{\partial \mathbf{m}}{\partial x} \times \frac{\partial \mathbf{m}}{\partial y}\right) \cdot \mathbf{m}\right\} dxdy$ the topological charge with $\mathbf{m}(x, y)$ the magnetic moment at position (x, y). μ_{B} and $\hbar$ are the Bohr magneton and the reduced Planck constant.

Gyromagnetic vector in a ferrimagnet. In a ferrimagnet such as TmIG, the effective γ can be computed from the saturation magnetization $M_{\mathrm{s,i}}$ and the gyromagnetic factors γ_i of the constituent sublattices (see Supplementary Eq. (3)), leading to[11,17]

$$\gamma = \frac{M_s}{\frac{M_{\mathrm{s},1}}{\gamma_1} - \frac{M_{\mathrm{s},2}}{\gamma_2}}. \tag{6}$$

In our TmIG films $\gamma < 0$ (see Supplementary Note 4), resulting in $G > 0$ for $Q = +1$ skyrmions. Note that Supplementary Eq. (5) can be rewritten as $G = 4\pi t s_{\mathrm{net}} Q$ with $s_{\mathrm{net}} = -\left(\frac{M_{\mathrm{s},1}}{\gamma_1} - \frac{M_{\mathrm{s},2}}{\gamma_2}\right) = -\frac{M_{\mathrm{s}}}{\gamma}$.

Skyrmion Hall angle. The skyrmion deflection angle ϕ_{sk} induced by the Magnus force $\mathbf{G} \times \mathbf{v}_{\mathrm{sk}}$ is given by[14,16,18]

$$\phi_{\mathrm{sk}} \sim \tan^{-1}\left(\frac{G}{\alpha' \mathcal{D}}\right), \tag{7}$$

where the components of the dissipative tensor $\boldsymbol{\mathcal{D}}$ are given by[14,16] $\mathcal{D}_{ij} = -s_{\mathrm{net}} t \iint \left\{\frac{\partial \mathbf{m}}{\partial i} \cdot \frac{\partial \mathbf{m}}{\partial j}\right\} dxdy$, with $\mathcal{D}'_{12} = \mathcal{D}'_{21} = 0$ and $\mathcal{D}'_{11} = \mathcal{D}'_{22} \approx -s_{\mathrm{net}} t \frac{2\pi R}{\Delta_{\mathrm{DW}}}$ under the approximation $R \gg \Delta_{\mathrm{DW}}$, with R and Δ_{DW} being the radius of and domain wall with of the skyrmion bubble[19,20]. α' is the effective damping and is given by[17]

$$\alpha' = \alpha \frac{s_{\mathrm{tot}}}{s_{\mathrm{net}}}, \tag{8}$$

with $s_{\mathrm{tot}} = -\left(\frac{M_{\mathrm{s},1}}{\gamma_1} + \frac{M_{\mathrm{s},2}}{\gamma_2}\right)$ the total angular momentum. By rewriting Supplementary Eq. (7) using the relations given above we obtain $\phi_{\mathrm{sk}} \sim \tan^{-1}\left(-\frac{s_{\mathrm{net}}}{s_{\mathrm{tot}}} \frac{2Q\Delta}{\alpha R}\right)$ as given in Eq. (1) of the main text. Note that

because $\frac{s_{net}}{s_{tot}}$ is negative in TmIG, ϕ_{sk} is positive (negative) for $Q = +1(-1)$ skyrmion bubbles as opposed to skyrmions in ferromagnets (see Supplementary Fig. 8 and Fig. 3 of the main text).

Skyrmion velocity. The skyrmion velocity $\boldsymbol{v}_{sk} = v_x\hat{\boldsymbol{x}} + v_y\hat{\boldsymbol{y}}$ in the flow regime is given by[16,21]

$$v_x = \frac{\eta}{1+\eta^2}\frac{F_{SOT}}{G}, \text{ and } v_y = \frac{1}{1+\eta^2}\frac{F_{SOT}}{G}, \tag{9}$$

and hence,

$$v_{sk} = |\boldsymbol{v}_{sk}| = \frac{1}{\sqrt{1+\eta^2}}\frac{F_{SOT}}{G}, \tag{10}$$

where

$$\eta = \frac{\alpha' D}{G} = -\frac{s_{tot}}{s_{net}}\frac{\alpha R}{2\Delta_{DW} Q} \quad \text{and} \quad \frac{F_{SOT}}{G} = -\xi_{DL} J_x \gamma \frac{\pi R}{4}, \tag{11}$$

with ξ_{DL} the effective field (per unit current density) associated to the damping-like SOT. Considering the values of ξ_{DL} reported for TmIG/Pt (Refs. 4,22), we estimate a skyrmion mobility $\eta = v_{sk}/J_x$ exceeding 3×10^{-8} m^3 A^{-1} s^{-1} in our TmIG devices, a value that is comparable to the mobility of ferrimagnetic domain walls near the angular momentum compensation[3,17,22,23,24].

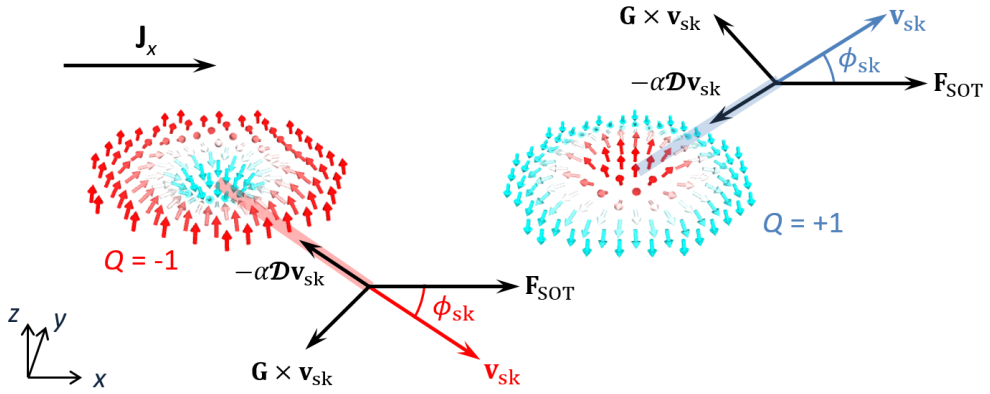

Supplementary Figure 8 | Schematic of the skyrmion Hall effect in TmIG. Schematics of $Q = -1$ and $Q = +1$ right-handed Néel skyrmion bubbles in TmIG and of the forces acting on the skyrmions due to the application of current pulses. The coordinate system and the direction of the current ($\mathbf{J}_x$), the skyrmion velocity ($\mathbf{v}_{sk}$), the sign of the deflection angle (ϕ_{sk}), and the forces acting on the skyrmions (see Supplementary Eq. (4)) are indicated. The vectors indicate the direction of the magnetic moments. As the sign of $\mathbf{G}$ is positive (negative) for $Q = +1$ (-1) skyrmion bubbles, the sign of ϕ_{sk} in TmIG is opposite to the one encountered in ferromagnetic materials.

Supplementary Note 6. Magnetic field dependence of the skyrmion radius.

The average skyrmion radius is analyzed from MOKE measurements taken on isolated bubbles and for different values of H_z (Extended Data Fig. 1). We note that the average radius inferred from the MOKE analysis (Extended Data Fig. 1c) is consistent with the radius extracted from NV magnetometry measurements (Fig. 2a-c of the manuscript). Both the increase of the bubble radius (Extended Data Fig. 1c) and the destabilization of the bubble domains into stripe domains when decreasing $|H_z|$ (Fig. 1d of the manuscript) are a consequence of the minimization of the magnetostatic energy of the bubble with field[25]. For fields below $|H_z| \lesssim 10$ Oe we cannot find only skyrmion bubbles by either current or field sweep protocols as the bubbles tend to expand and transform into stripe domains.

Supplementary Note 7. Skyrmion deformations due to pinning

Skyrmion ellipticity. The statistical analysis of the bubbles' shape extracted from MOKE data show that most skyrmion bubbles present an ellipticity $b/a \gtrsim 0.9$ (Extended Data Figs. 1a and 2a), indicating that the bubbles tend to retain a circular shape after a current pulse. a and b define the larger and smaller axes of the ellipsoid. Such ellipsoidal deformations correspond to relative contractions/elongations of the skyrmion diameter of about 50 ± 50 nm between each other. These results are consistent with an average distance between pinning centers of about 50 to 100 nm if the deformations are assumed to arise from the hopping of the skyrmion wall between two adjacent defects.

Current-induced bubble deformations. We found a correlation between the most preferred direction of bubble deformation relative to the direction of the current pulses. Concretely, we found that the bubbles exhibit a larger probability to exhibit deformation in the direction of motion as well as perpendicular to it (Extended Data Fig. 2b). Whereas the former indicates that the deformations correlate with the direction of skyrmion motion set by the skyrmion Hall effect and pinning[20,26,27], the latter is consistent with bubble distortions induced by SOTs[28].

Supplementary Note 8. Alternative explanations for the pulse length dependence: inertial and automotion effects

Inertial effects. A possible explanation for the finite bubble displacements observed as $t_{\mathrm{p}} \to 0$ (Fig. 4c,d of the main text as well as Extended Data Figs. 5 and 6) is that the skyrmion bubbles behave as objects with a finite mass and thus keep moving after the end of a current pulse. This effect would be detected in MOKE experiments if there is an asymmetry in the acceleration and deceleration times of the skyrmion bubbles, as reported for Néel domain walls in low-damping media and moderate DMI[29]. However, such inertia effects are expected to emerge for domain walls and skyrmions driven in the flow regime. In the presence of random hopping produced by disorder and thermal fluctuations, as observed in our experiments for skyrmion bubbles driven in the creep regime (Figs. 4 and 5 of the main text), we expect that the inertia effects would be negligible.

Automotion. Another explanation for the pulse length dependence of $\overline{\Delta x}$, $\overline{\Delta y}$ and $\bar{v}_{\mathrm{sk}}$ (Fig. 4c-e of the main text) is that the skyrmion bubbles exhibit automation effects as the result of the displacement of vertical Bloch lines around the bubble boundary, in analogy with the behaviour of magnetic bubbles in a field gradient observed in thick garnet layers[16,30,31]. The displacement of vertical Bloch lines would be driven by the reversal of $\mathbf{M}_{\mathrm{YIG}}$ induced by the in-plane Oersted fields generated by the pulses ($\mathbf{H}_{\mathrm{Oe,y}} \propto +J_{\mathrm{x}}\hat{\mathbf{y}}$ at the YIG plane), and therefore inertia effects may only emerge for one polarity of $\mathbf{J}_{\mathrm{x}}$ for a given $\mathbf{M}_{\mathrm{YIG}}||\boldsymbol{y}$ configuration. This scenario, however, is ruled out because a similar behaviour is observed for all orientations of $\mathbf{M}_{\mathrm{YIG}}$ and $\mathbf{J}_{\mathrm{x}}$. Extended Data Figure 6 shows representative data taken for $\mathbf{M}_{\mathrm{YIG}} = -M_{\mathrm{YIG}}\hat{\mathbf{y}}$, revealing finite displacements for both polarities of $\mathbf{J}_{\mathrm{x}}$ as $t_{\mathrm{p}} \to 0$. In addition, analysis of the current threshold for bubble depinning as function of $\mathbf{J}_{\mathrm{x}}$ amplitude, in-plane field H_{y}, and pulse length t_{p} suggests that the in-plane Oersted fields are not capable to produce significant changes to $\mathbf{M}_{\mathrm{YIG}}$ (Supplementary Note 9), which we ascribe to the relatively large thickness of TmIG and the moderate current densities employed in the experiments.

Supplementary Note 9: Influence of the Oersted field and H_y on the skyrmion dynamics

As demonstrated in Figs. 5 and 6 of the manuscript, both the skyrmion depinning probability and the velocity of the skyrmion bubbles strongly depend on the orientation of $\mathbf{M}_{\mathrm{YIG}}$ relative to $\mathbf{J}_x$. To control the orientation of $\mathbf{M}_{\mathrm{YIG}}$, a small in-plane magnetic field $\mathbf{H}_y = H_y\hat{\boldsymbol{y}}$ is applied (see Supplementary Note 2 for more details regarding the magnetic properties of the films; in particular, Supplementary Fig. 3b shows that an in-plane field as small as 3 Oe can significantly modify $\mathbf{M}_{\mathrm{YIG}}$). It is therefore crucial to determine whether the asymmetry in the dynamics of the skyrmion bubbles with $\mathbf{J}_{\mathrm{x}}$ may arise from the influence of the in-plane Oersted field $\mathbf{H}_{\mathrm{Oe},y} = H_{\mathrm{Oe},y}\hat{\boldsymbol{y}} \propto +J_{\mathrm{x}}\hat{\boldsymbol{y}}$ generated by the pulses on $\mathbf{M}_{\mathrm{YIG}}$, as well as to determine whether $\mathbf{H}_y$ itself influence the dynamics. To investigate these questions, we determined the current threshold J_x^{th} for skyrmion depinning as function of $\mathbf{J}_{\mathrm{x}}$ orientation, pulse length t_{p}, and H_y strength.

Supplementary Figure 9 shows representative data taken for $H_y < 0$ and $Q = +1$ ($H_z = -20$ Oe). At magnetic fields below $|H_y| \sim 4$ Oe, the current threshold is rather independent on the magnetic field and the polarity of the current, but above that field value, a strong asymmetry with $\mathbf{J}_x$ emerges, with the current threshold becoming larger for J_x < 0, an asymmetry that is in agreement with the results presented in Fig. 6e,f of the main text. Moreover, when reversing the direction of H_y (not shown here), we observe that the current threshold becomes larger for J_x > 0, while it stays rather constant for J_x < 0, also in agreement with the asymmetry with $\mathbf{J}_{\mathrm{x}}$ for $\mathbf{M}_{\mathrm{YIG}} = +M_{\mathrm{YIG}}\hat{\boldsymbol{y}}$ presented in Fig. 6g,h of the main text (see Supplementary Note 10 for more details regarding the asymmetries of the ratchet effect). We note that the results shown in Supplementary Fig. 9 are not dependent on the particular sequence followed with the magnetic field $\mathbf{H}_y$ before starting the measurements, suggesting that the application of current pulses randomize the domains towards the equilibrium configuration set by the external field for values in the range $|H_y| < -10$ Oe.

The rather constant J_x^{th} with $H_y < 0$ observed for $J_x > 0$ (Supplementary Fig. 9b) is attributed to the fact that no significant difference should be observed in J_x^{th} between a demagnetized case ($H_y = 0$ Oe) and a saturated one along the favoured $\mathbf{M}_{\mathrm{YIG}}$ direction. That is because a demagnetized case presents domains with both favoured and unfavoured $\mathbf{M}_{\mathrm{YIG}}$ orientations as well as intermediate ones aligned with the current. The average skyrmion velocity for $J_x > 0$, however, increases when $\mathbf{M}_{\mathrm{YIG}}$ saturates along $-\boldsymbol{y}$, in agreement with the data shown in Figs. 4a,b and 5a,b of the main text. Further, the velocity is found to be weakly dependent on the external field for fields from $|H_y| \sim -10$ Oe to ~ -25 Oe, the later defining the threshold for the destabilization of the bubble domains into stripe domains.

We now focus our attention on the field dependence of the current threshold for $J_x < 0$ and $H_y < 0$ (Supplementary Fig. 9a). Remarkably, while the depinning current density increases by a factor ~ 4 when decreasing the pulse length from 100 to 15 ns (blue up triangles and green down triangles, respectively; note that the t_{p}-dependence of J_x^{th} is in agreement with the data presented in Extended Data Fig. 3), the field-dependence remains qualitatively the same, with a field-independent regime

observed from $|H_y| \sim 10$ to 20 Oe. The fact that the field independent regime is reached at the same value for all current conditions (despite the associated $H_{\mathrm{Oe},y}$ field differs by a factor ~ 4 between the extreme cases: $J_x \sim 8.5 \times 10^{11}$ A m^{-2} for $t_\mathrm{p} = 15$ ns, while $J_x \sim 2.2 \times 10^{11}$ A m^{-2} for $t_\mathrm{p} = 100$ ns), indicates that the influence of $\mathbf{H}_{\mathrm{Oe},y}$ on $\mathbf{M}_\mathrm{YIG}$ is negligible and that the magnetization of the YIG film is saturated above $|H_y| = H_s = 10$ Oe (indicated by a vertical line), further indicating that H_y has a negligible effect on the skyrmion dynamics compared to $\mathbf{M}_\mathrm{YIG}$. We thus conclude that the ratchet effect arises from the exchange coupling of $\mathbf{M}_\mathrm{YIG}$ with the skyrmions in TmIG.

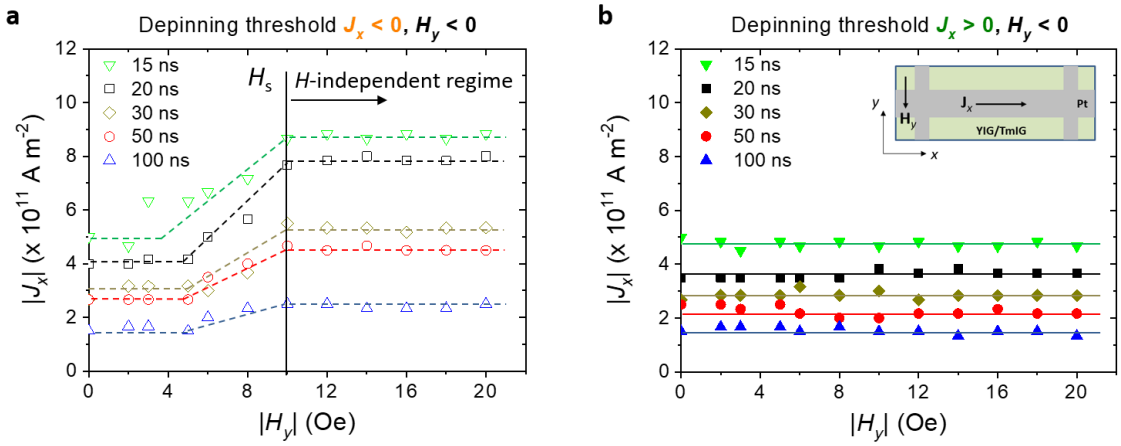

Supplementary Figure 9 | Current threshold for the depinning of skyrmion bubbles as function of $\mathbf{J_x}$, $\boldsymbol{t_\mathrm{p}}$, and $\boldsymbol{H_y}$. **a**, Current threshold as function of H_y for different pulse lengths. The polarity of the magnetic field and the current applied are $H_y < 0$ and $J_x < 0$, which corresponds to the unfavoured configuration for bubble motion. Same field dependence is observed for $H_y > 0$ and $J_x > 0$. The dashed lines are guides to the eye. A field-independent regime is reached at $H_\mathrm{s} \sim 10$ Oe for all t_p, $|J_x|$ conditions (indicated with a vertical solid line). **b**, Same as **a**, but for $J_x > 0$ and $H_y < 0$, i.e., a favoured configuration for skyrmion motion. Same data is obtained for $J_x < 0$ and $H_y > 0$. The solid lines are guides to the eye. Data in **a** and **b** correspond to $Q = +1$ skyrmion bubbles with $H_z = -20$ Oe. Same behaviour for the current depinning threshold is observed for $Q = -1$ skyrmion bubbles and $H_z = +20$ Oe. The inset indicates the orientation of $\mathbf{J}_x$ and $\mathbf{H}_y$ relative to the current line. See Supplementary Note 10 and Figs. 5 and 6 of the main text for more details regarding the symmetries of the skyrmion dynamics with $\mathbf{M}_\mathrm{YIG}$, $\mathbf{J}_x$, and Q.

Supplementary Note 10. Skyrmion ratchet effect: supplementary data

Q	$\mathbf{M}_{\mathrm{YIG}}(\hat{\boldsymbol{y}})$	$\mathbf{J}_x(\hat{\boldsymbol{x}})$	$\mathbf{T}^{\mathrm{DL}}(\hat{\boldsymbol{y}})$	$\lvert\mathbf{v}_{\mathrm{sk}}\rvert$	Ratchet ($\hat{x}$)
+/−	Demag	+/−		Intermediate	No
+/−	−	+	+	Fast	+
+/−	−	−	−	Slow or pinned	
+/−	+	+	+	Slow or pinned	−
+/−	+	−	−	Fast	

Supplementary Table 1 | Skyrmion dynamics with $\mathbf{M}_{\mathrm{YIG}}$, $\mathbf{J}_x$, and Q: symmetry of the ratchet effect. Comparison of the skyrmion dynamics for different $\mathbf{M}_{\mathrm{YIG}}$, $\mathbf{J}_x$, and Q configurations relative to the YIG demagnetized case. The vectors $\hat{\boldsymbol{x}}$ and $\hat{\boldsymbol{y}}$ indicate the orientation of the vectors $\mathbf{M}_{\mathrm{YIG}}$, $\mathbf{J}_x$, $\mathbf{T}^{\mathrm{DL}}$, and the ratchet effect, and the sign + or − their polarity (see Fig. 1a of the main text for the definition of the sample coordinates). Note that the polarity of $\mathbf{T}^{\mathrm{DL}}$ is given by $\mathbf{J}_x$ and that here we only consider the sign of the $\hat{\boldsymbol{y}}$ component at the bubbles wall as is the relevant one for the ratchet effect. Further, we only consider configuration with $\mathbf{M}_{\mathrm{YIG}}$ orthogonal to $\mathbf{J}_x$ as no asymmetry in the dynamics is observed when $\mathbf{M}_{\mathrm{YIG}}$ and $\mathbf{J}_x$ are collinear (Extended Data Fig. 7). When the polarity of $\mathbf{J}_x(\hat{\boldsymbol{x}})$ and $\mathbf{M}_{\mathrm{YIG}}(\hat{\boldsymbol{y}})$ are the same, the dynamics of the skyrmions are slow or pinned (combinations indicated by orange colour), but when they are opposite, the skyrmion motion is efficient and faster (indicated by green colour) relative to the demagnetized case. See also Figs. 5 and 6 of the main text, which present representative data of the dynamics of the skyrmion bubbles with $\mathbf{J}_x(\hat{\boldsymbol{x}})$ and $\mathbf{M}_{\mathrm{YIG}}(\hat{\boldsymbol{y}})$. For a given $\mathbf{M}_{\mathrm{YIG}}(\hat{\boldsymbol{y}})$ orientation, the asymmetry in the skyrmion dynamics with $\mathbf{J}_x(\hat{\boldsymbol{x}})$ leads to the ratchet effect indicated in the last column, with the bubble motion being preferred towards $+\hat{\boldsymbol{x}}$ for $\mathbf{M}_{\mathrm{YIG}}$ aligned to $-\hat{\boldsymbol{y}}$, while motion is preferred towards $-\hat{\boldsymbol{x}}$ for $\mathbf{M}_{\mathrm{YIG}}$ saturated along $+\hat{\boldsymbol{y}}$ (note that here the deflection of the skyrmion bubbles towards $\pm\hat{\boldsymbol{y}}$ due to the topological Hall effect is not considered for simplicity). The same asymmetric motion is observed for both $Q = +1$ and -1 skyrmion bubbles. As schematized in Fig. 6a-d of the main text, the asymmetric dynamics with $\mathbf{J}_x$ originates from the distortion of the magnetic configuration of the skyrmion bubbles produced by $\mathbf{T}^{\mathrm{DL}}$ (which depends on $\mathbf{J}_x$) relative to the one induced by the exchange coupling with $\mathbf{M}_{\mathrm{YIG}}$. When the distortions oppose (favour) each other, the net distortion towards $\hat{\boldsymbol{y}}$ becomes smaller (larger), resulting in stronger (weaker) $\mathbf{F}_{\mathrm{SOT}}$ driving forces. See also Supplementary Fig. 10, which provide additional sketches of the expected distortion of the skyrmion bubbles for other $\mathbf{M}_{\mathrm{YIG}}$, $\mathbf{J}_{\mathrm{x}}$, and Q configurations than the ones presented in Fig. 6a-d of the main text.

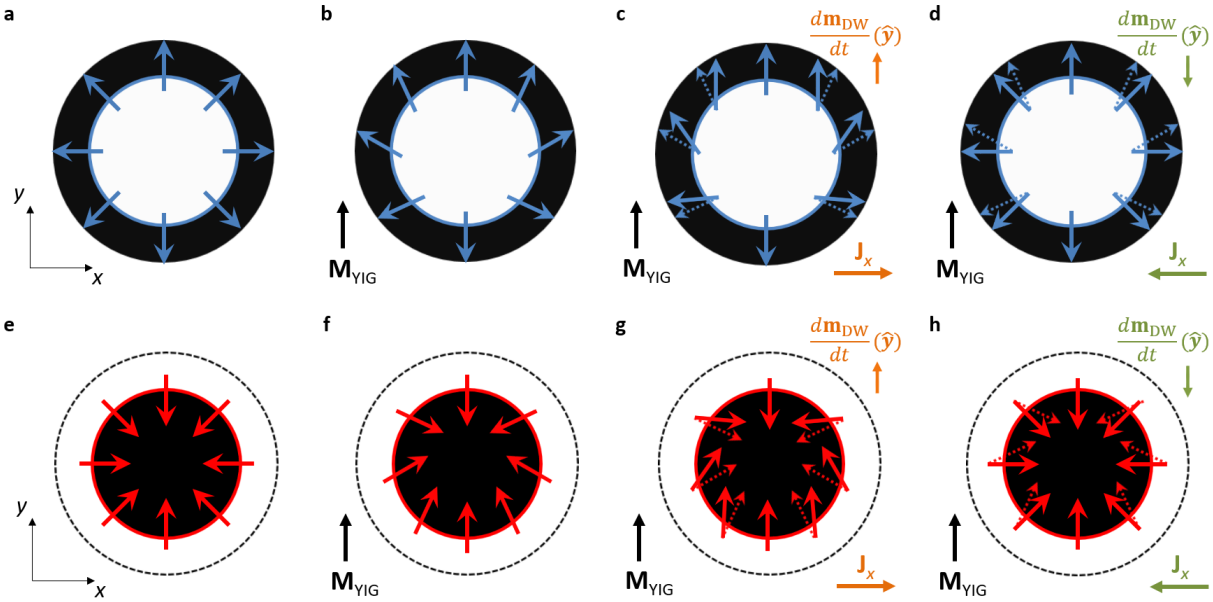

Supplementary Figure 10 | Schematics of the magnetic distortion of the skyrmion bubbles with $\mathbf{M}_{\mathrm{YIG}}$ and $\mathbf{J}_x$: additional $\mathbf{M}_{\mathrm{YIG}}$ and Q configurations. a-d, Same as Fig. 6a-d of the main text, but for $\mathbf{M}_{\mathrm{YIG}} = +M_{\mathrm{YIG}}\hat{\boldsymbol{y}}$. As opposed to the case of Fig. 6a-d, the distortion of the skyrmion bubble is enhanced (reduced) for $J_x > 0$ ($J_x < 0$). Consequently, for $\mathbf{M}_{\mathrm{YIG}} = +M_{\mathrm{YIG}}\hat{\boldsymbol{y}}$ the skyrmion motion is more efficient for $J_x < 0$ than for $J_x > 0$, in agreement with the results presented in Fig. 6g,h of the main text. **e-h**, Same as **a-d**, but for a $Q = -1$ skyrmion bubble. The symmetry of the resulting torques with $\mathbf{J}_x$ is the same as for $Q = +1$ skyrmion bubbles, i.e., larger (smaller) distortions are observed for $J_x > 0$ ($J_x < 0$). See **c**,**d** and **g**,**h**. In the later, only the direction of the $\hat{\boldsymbol{y}}$ component of the $d\mathbf{m}_{\mathrm{DW}}/dt$ induced by the torques is depicted for simplicity. Fast (slow) motion is expected when $d\mathbf{m}_{\mathrm{DW}}/dt(\hat{\boldsymbol{y}})$ opposes $\mathbf{M}_{\mathrm{YIG}}$.

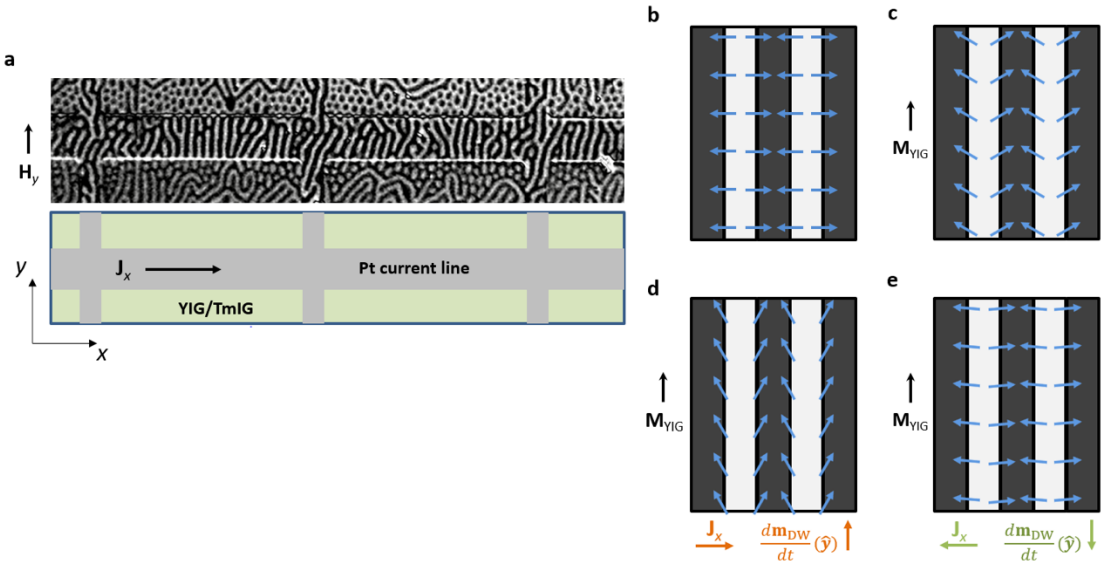

Supplementary Figure 11 | Ratchet effect for stripe domains. a, *Top*, Differential MOKE image showing stripe domains in TmIG. The white (dark) contrast indicates domains with the magnetization pointing up (down). An in-plane magnetic field $H_y = +30$ Oe is applied along $+\hat{\boldsymbol{y}}$ to stabilize stripe domains oriented perpendicular to the current line. $H_z = -10$ Oe. *Bottom*, Schematics indicating the position of the current line in the MOKE image. When applying current pulses $\mathbf{J}_x$, as for the case of skyrmion bubbles with $\mathbf{M}_{\mathrm{YIG}} = +M_{\mathrm{YIG}}\hat{\boldsymbol{y}}$, we observe that the dynamics of the stripe domains is more efficient for $J_x < 0$ than for $J_x > 0$ (see Fig. 6g,h of the main text). When the orientation of $\mathbf{H}_y$ is reversed, the asymmetry in the dynamics of the stripe domains with $\mathbf{J}_x$ is also reversed, agreeing with the asymmetry with $\mathbf{M}_{\mathrm{YIG}}$ (which is set by $\mathbf{H}_y$) and $\mathbf{J}_x$ as summarized in Supplementary Table 1. The explanation of the effect is the same as for the case of skyrmion bubbles. The motion of the stripe domains is more (less) efficient when the distortion of the magnetic moments at the stripe's walls by $\mathbf{M}_{\mathrm{YIG}}$ and $\mathbf{J}_x$ is minimal (maximal). See sketches from **b** to **e**. The bubble domains surrounding the current line are induced by the out of plane component of the Oersted field for currents $\mathbf{J}_x \gtrsim 8 \times 10^{11}$ A m^{-2} at this field values. **b**, Schematics of the expected orientation of the magnetic moments at the walls of the stripe domains in TmIG (as discussed in the main text, the domain walls should exhibit right-handed Néel chirality). **c**, Magnetic distortion of the walls due to $\mathbf{M}_{\mathrm{YIG}} = +M_{\mathrm{YIG}}\hat{\boldsymbol{y}}$. **d**, **e**, Additional magnetic distortion due to $\mathbf{J}_x$, showing that a more efficient wall motion is expected for $J_x > 0$ (**d**) than for $J_x < 0$ (**e**).

References

1. Mendil, J. *et al.* Magnetic properties and domain structure of ultrathin yttrium iron garnet/Pt bilayers. *Phys. Rev. Mater.* **3**, 034403 (2019).
2. Espinosa, G. P. Crystal chemical study of the rare-earth iron garnets. *J. Chem. Phys.* **37**, 2344–2347 (1962).
3. Vélez, S. *et al.* High-speed domain wall racetracks in a magnetic insulator. *Nat. Commun.* **10**, 4750 (2019).
4. Avci, C. O. *et al.* Current-induced switching in a magnetic insulator. *Nat. Mater.* **16**, 309–314 (2017).
5. Nakayama, H. *et al.* Spin Hall Magnetoresistance Induced by a Non-Equilibrium Proximity Effect. *Phys. Rev. Lett.* **110**, 206601 (2013).
6. Isasa, M. *et al.* Spin Hall Magnetoresistance as a Probe for Surface Magnetization in Pt/CoF2O4 Bilayers. *Phys. Rev. Appl.* **6**, 034007 (2016).
7. Collet, M. *et al.* Generation of coherent spin-wave modes in yttrium iron garnet microdiscs by spin-orbit torque. *Nat. Commun.* **7**, 10377 (2016).
8. Tetienne, J. P.-P. *et al.* The nature of domain walls in ultrathin ferromagnets revealed by scanning nanomagnetometry. *Nat. Commun.* **6**, 6733 (2015).
9. Dovzhenko, Y. *et al.* Magnetostatic twists in room-temperature skyrmions explored by nitrogen-vacancy center spin texture reconstruction. *Nat. Commun.* **9**, 2712 (2018).
10. Lemesh, I., Büttner, F. & Beach, G. S. D. Accurate model of the stripe domain phase of perpendicularly magnetized multilayers. *Phys. Rev. B* **95**, 174423 (2017).
11. Wangsness, R. K. Sublattice Effects in Magnetic Resonance. *Phys. Rev.* **91**, 1085–1091 (1953).
12. Paulevé, J. Ferromagnetic Resonance of Gadolinium Garnet at 9300 MC/S. *C. R. Acad. Sci.* **244**, 1908 (1957).
13. Shao, Q. *et al.* Role of dimensional crossover on spin-orbit torque efficiency in magnetic insulator thin films. *Nat. Commun.* **9**, 3612 (2018).
14. Nagaosa, N. & Tokura, Y. Topological properties and dynamics of magnetic skyrmions. *Nat. Nanotechnol.* **8**, 899–911 (2013).
15. Thiele, A. A. Steady-State Motion of Magnetic Domains. *Phys. Rev. Lett.* **30**, 230–233 (1973).
16. Zang, J., Cros, V. & Hoffmann, A. *Topology in Magnetism, Chapter 2*. (Springer, 2019).
17. Caretta, L. *et al.* Fast current-driven domain walls and small skyrmions in a compensated ferrimagnet. *Nat. Nanotechnol.* **13**, 1154–1160 (2018).
18. Zhang, X., Zhou, Y. & Ezawa, M. Magnetic bilayer-skyrmions without skyrmion Hall effect. *Nat. Commun.* **7**, 10293 (2016).
19. Hrabec, A. *et al.* Current-induced skyrmion generation and dynamics in symmetric bilayers. *Nat. Commun.* **8**, 15765 (2017).
20. Hirata, Y. *et al.* Vanishing skyrmion Hall effect at the angular momentum compensation temperature of a ferrimagnet. *Nat. Nanotechnol.* **14**, 232–236 (2019).
21. Juge, R. *et al.* Current-Driven Skyrmion Dynamics and Drive-Dependent Skyrmion Hall Effect in an Ultrathin Film. *Phys. Rev. Appl.* **12**, 044007 (2019).
22. Avci, C. O. *et al.* Interface-driven chiral magnetism and current-driven domain walls in insulating magnetic garnets. *Nat. Nanotechnol.* **14**, 561–566 (2019).
23. Siddiqui, S. A., Han, J., Finley, J. T., Ross, C. A. & Liu, L. Current-Induced Domain Wall Motion in a Compensated Ferrimagnet. *Phys. Rev. Lett.* **121**, 057701 (2018).
24. Kim, K. J. *et al.* Fast domain wall motion in the vicinity of the angular momentum

compensation temperature of ferrimagnets. *Nat. Mater.* **16**, 1187–1192 (2017).

25. Wu, H. *et al.* Ferrimagnetic Skyrmions in Topological Insulator/Ferrimagnet Heterostructures. *Adv. Mater.* **32**, 2003380 (2020).
26. Zeissler, K. *et al.* Diameter-independent skyrmion Hall angle observed in chiral magnetic multilayers. *Nat. Commun.* **11**, 428 (2020).
27. Kim, J.-V. & Yoo, M.-W. Current-driven skyrmion dynamics in disordered films. *Appl. Phys. Lett.* **110**, 132404 (2017).
28. Litzius, K. *et al.* The role of temperature and drive current in skyrmion dynamics. *Nat. Electron.* **3**, 30–36 (2020).
29. Torrejon, J., Martinez, E. & Hayashi, M. Tunable inertia of chiral magnetic domain walls. *Nat. Commun.* **7**, 13533 (2016).
30. Slonczewski, J. C., Malozemoff, A. P. & Voegeli, O. Statics and Dynamics of Bubbles Containing Bloch Lines. *AIP Conf. Proc.* **10**, 458 (2008).
31. Tabor, W. J., Bobeck, A. H., Vella-Coleiro, G. P. & Rosencwaig, A. A New Type of Cylindrical Magnetic Domain (Hard Bubble). *AIP Conf. Proc.* **10**, 442–457 (1973).